IIETA International Information and Engineering Technology Association
Advancing the World of Information and Engineering

Traitement du Signal
Vol. 41, No. 3, June, 2024, pp. 1527-1537
Journal homepage: http://iieta.org/journals/ts

Enhanced Methodology for Building Surface Inspection Using Infrared Thermography and Numerical Simulation

Ming Bao[1], Na Zhang[2*]

[1] School of Architecture, Inner Mongolia University of Technology, Hohhot 010051, China
[2] School of Electrical Engineering, Inner Mongolia University of Technology, Hohhot 010051, China

Corresponding Author Email: zhangna@imut.edu.cn

https://doi.org/10.18280/ts.410340

Received: 15 January 2024
Revised: 6 April 2024
Accepted: 12 May 2024
Available online: 26 June 2024

Keywords:
infrared thermography (IRT), ANSYS Fluent, building surface inspection, heat transfer modeling, numerical simulation

ABSTRACT

This study presents an advanced methodology for assessing building surfaces by integrating infrared thermography (IRT) with ANSYS Fluent numerical simulation. IRT was employed to gather thermal characterization data of building surfaces under varying environmental conditions, comparing structures in both campus and urban settings. Subsequently, a three-dimensional heat transfer model was developed using ANSYS Fluent to simulate the thermal properties of building surfaces under different operational scenarios and validate the experimental findings. The analysis investigated the effects of building surface size, depth, and positioning on thermal insulation efficiency. Experimental results indicated that insulation distribution on campus building surfaces appeared more dispersed under IRT, suggesting a higher likelihood of thermal anomalies. Numerical simulations with ANSYS Fluent demonstrated that increasing the surface area of buildings enhances resistance to heat transfer, thereby diminishing the insulation effectiveness. This study provides a comprehensive performance assessment approach by seamlessly combining experimental testing with numerical simulation, offering novel insights and methodologies for building surface inspection and evaluation.

1. INTRODUCTION

As urbanization accelerates and building technology advances, detecting and monitoring building facades becomes increasingly crucial [1]. The temperature distribution information on a building façade not only represents the structure's operating status, but it also provides important data for energy management and environmental monitoring [2]. Because of its great efficiency, non-contact nature, and all-weather capabilities, IRT is commonly used to monitor building façade temperatures [3]. However, typical IRT can only offer temperature distribution information and does not combine building façade texture information with visual pictures, limiting its use in building structure study and management [4].

Building thermography can accurately depict the thermal distribution and energy performance of structures by monitoring infrared radiation on building surfaces [5]. However, due to the variety of building materials and the surrounding environment, thermal imaging data frequently contains noise and artifacts, reducing the precision and reliability of temperature distribution [6]. Traditional signal processing approaches, while capable of reducing noise, are nonetheless challenged by complex backgrounds and uncertainty [7].

Machine learning approaches, particularly deep learning-based algorithms, can better reduce noise in thermal imaging data and extract more relevant information by learning features and patterns from huge amounts of data [8, 9].

Although machine learning algorithms show promise in thermal imaging data processing, they still confront significant obstacles in practical applications [10]. First, the complexity and diversity of building thermal imaging data necessitate machine learning models with strong generalization capabilities to handle data from many types of buildings and climatic situations [11]. Second, how to properly pick and process a large amount of training data, as well as construct an appropriate model structure, are critical elements influencing the noise reduction effect and improved analysis capabilities [12].

Furthermore, to fully comprehend the building's performance and operational status, a fine-grained analysis of thermal imaging data must include information from many areas, such as the building's physical structure and energy consumption pattern [13]. As a result, how to effectively integrate and use multi-source data to improve the use of machine learning models in the refined analysis of building technologies is an essential area for future research.

To address this restriction, this work presents an alignment and texture mapping method based on IRT and RGB pictures to achieve temperature texture remapping of building facades [14]. In contrast to previous approaches, we apply the Shifting Structure Tool (SfM) and Fast Global Alignment (FGR) algorithms to align thermal and RGB pictures before combining them with the Invariant Emission Feature Transform. Accurate and robust feature matching can be achieved using methods such as feature transform (RIFT),

normalized center-of-mass coordinate system (NBCS), and randomly sampled sequences (RANSAC) [15]. In addition, we present a global posture refinement method to enhance the geometric correctness of texture mapping.

The research significance of this study is mostly represented in the following areas:

First, the integration of infrared thermal imaging and RGB photos achieves an organic combination of temperature distribution and visual texture information of building facades, resulting in more comprehensive and accurate analytical data for the operational state of buildings.

Second, the suggested method efficiently maps the temperature properties of thermal pictures onto the RGB point cloud model, opening up new avenues for temperature monitoring and analysis of building facades.

Third, the alignment and texture mapping methods suggested in this research are very accurate and resilient, capable of handling difficult scenarios in a variety of contexts, and provide dependable technical assistance for real-world engineering applications.

2. PROPOSED METHOD

2.1 Alignment work

The implemented alignment workflow is summarized in Figure 1: Initially, the infrared image is processed using a typical SfM program to create a second 3D point cloud, which is then aligned with the RGB image's point cloud. In order to get the approximate transformation information between these two point clouds, a quick global alignment procedure is then used. The optimal RGB image for every thermal image is determined by figuring out the exterior orientation parameters' minimum Euclidean distance. The Radiation Invariant Feature Transform (RIFT), Normalized Barry Central Coordinate System (NBCS), and RANSAC are then utilized to perform an accurate and trustworthy feature match on each chosen combination of RGB heatmap images. Finally, the relevant feature in the RGB image is used to determine the proper position. These spots are then deleted from the thermal image space in order to optimize their external orientation characteristics.

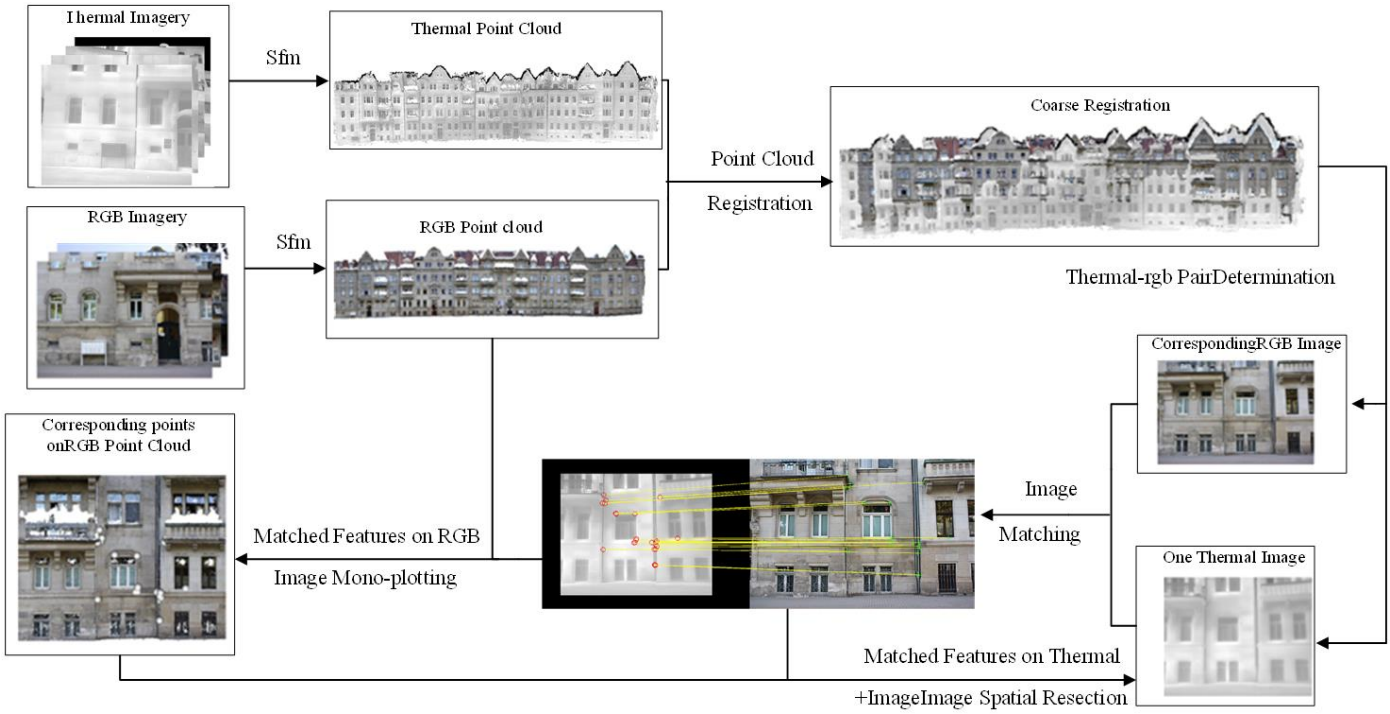

Figure 1. Registration workflow

2.1.1 Generation of point clouds

The thermal image and the RGB image were transformed into a hot spot cloud and an RGB point cloud, respectively, using a Structure in Motion (SfM) application (such as Agisoft PhotoScan®). The RGB were employed as a 3D reference since their resolution and contrast were far higher than the thermal images', but the thermal images supplied the appropriate temperature characteristics. The contrast of the thermal image needs to be improved before using the SfM tool to create the hotspot cloud. To do this, we apply a Wallis filter.

Iterative Nearest Point (ICP) and its variations are frequently used point cloud registration techniques. When the initialization criteria are met, these algorithms typically yield precise alignment information. However, this work does not provide such startup conditions. Furthermore, registering heterogeneous point clouds becomes more challenging due to the fact that thermal 3D point clouds are sparser and noisier than RGB point clouds [16]. As a result, the alignment technique employed must be capable of handling noisy data as well as initialization-independent information. The basic procedure is as follows: First, alter the RGB point cloud with a proportionality parameter that determines the minimum ratio of the border frame length on the XYZ axis, or $(\Delta X_{\text{Thermal}}/\Delta X_{RGB}, \Delta Y_{\text{Thermal}}/\Delta Y_{RGB}, \Delta Z_{\text{Thermal}}/\Delta Z_{RGB})$, because the scaling of thermal and RGB point clouds differs (Figure 2). This allows for the extraction of matching features on the same scale. Next, the first correspondence set was created using the features from the FPFH. The pairs that are closest to one another, and the tuple test, which confirms the correspondences' compatibility, are then used to exclude outliers from the correspondence set. Lastly, the coarse alignment results are estimated using RANSAC and FGR.

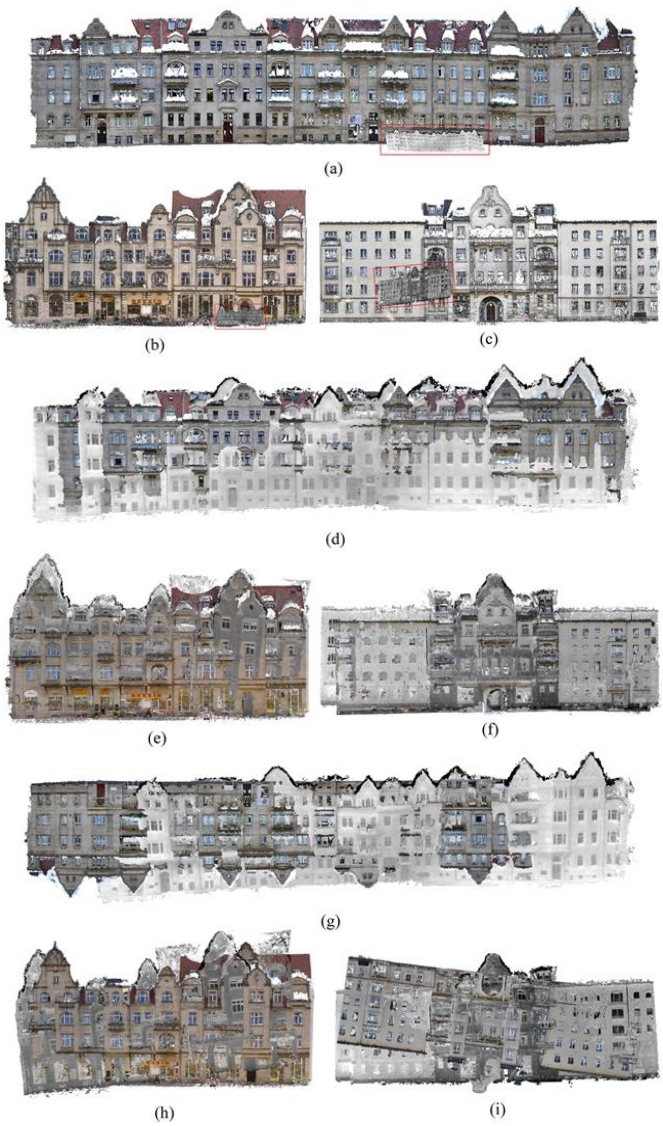

Figure 2. Point cloud coarse registration displays the point cloud's initial poses for elevations 1, 2, and 3. The matching FGR and RANSAC results are displayed in (d-f) and (g-i), respectively

FGR outperforms RANSAC when working with noisy feature correspondence sets from varied point clouds of varying densities and accuracies, as seen in Figure 2. This is because RANSAC occasionally converges to a local minimum. Since the scaled Geman-McClure estimator can reliably remove false correspondences during optimization, FGR employs it as a punishment function. Consequently, FGR outperforms RANSAC when handling noisy correspondence sets. It should be noted that although we attempted to use ICP to further optimize the FGR results, ICP was unable to increase the alignment's accuracy due to the disparate precision and density of heterogeneous point clouds. Elevation 1 measures approximately 100 meters in length and 26 meters in height; Elevation 2 measures approximately 51 meters in length and 22 meters in height; and Elevation 3 measures approximately 58 meters in length and 24 meters in height.

2.1.2 Image matching in thermal RGB

To create thermal texture maps, the thermal point cloud must be more finely registered with the RGB point cloud after the FGR coarse registration is finished. As a result, it is important to use a thermal-RGB image pair matching technique. According to the study [17], standard algorithms based on picture intensity and gradient (e.g., SIFT, SURF) frequently fail to find point correspondences in thermal-RGB image pairings. These techniques are limited to smaller linear intensity differences since they detect and characterize the feature points using the gradient information in the spatial domain, which makes them ineffective for handling the matching of thermal-RGB image pairings. However, thermal-RGB image pairs typically have significant nonlinear radiance discrepancies. On the other hand, the RIFT technique is more resilient when handling significant nonlinear radiation changes and uses phase coherence recognition. As a result, this paper uses the RIFT technique for feature characterisation and detection. Eq. (1) illustrates the metric to be used: The Euclidean distance between the exterior orientation parameters of the thermal and RGB images.

$$d = \left(X_{RGB} - X_T\right)^2 + \left(Y_{RGB} - Y_T\right)^2 + \left(Z_{RGB} - Z_T\right)^2 + \left(\frac{\omega_{RGB} - \omega_T}{p_{\omega\varphi x}}\right)^2 + \left(\frac{\varphi_{RGB} - \varphi_T}{p_{\omega\varphi x}}\right)^2 + \left(\frac{\kappa_{RGB} - \kappa_T}{p_{\omega\varphi x}}\right)^2 \quad (1)$$

where, $(X_{RGB} \quad Y_{RGB} \quad Z_{RGB})$ = FGR is the FGR-transformed RGB image's center of projection.

$(X_T \quad Y_T \quad Z_T)$ = the thermal image's projection center.

2.1.3 Calculating the image posture

To achieve exact matching of the heatmap and RGB point cloud, we take a simple two-step strategy. To extract 3D feature points from image coordinates corresponding to objects in RGB photos and the RGB point cloud, we first match each pair of heatmaps and RGB photographs separately. The exterior orientation parameters of each heatmap picture are then computed by inversely intersecting the spaces using the coordinates of the images corresponding to the features as well as the coordinates of the objects in the 3D point clouds.

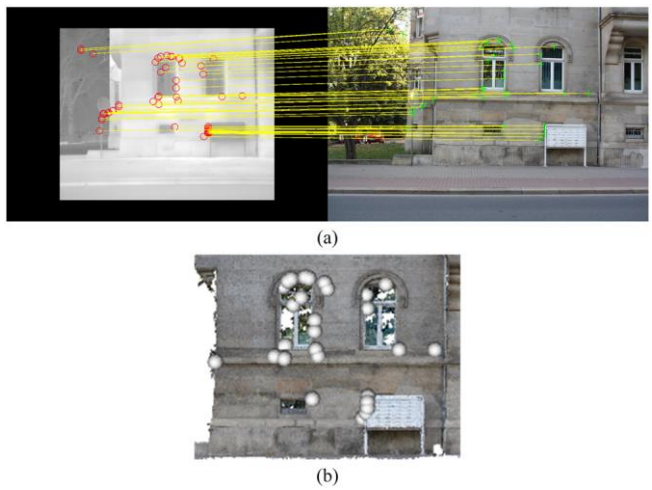

Figure 3. Image resection using non-elevation point removal (a) Correspondence matching between pairs of thermal and RGB images (b) The outcome of a single plotting, where the matching object points are represented by white spheres

Specifically, spatial subdivision is initially carried out to assign a small section of the elevation to each image depending on the center of projection during the single-labeling phase. The target object point is then found for each

picture feature (ray) by choosing the point among all assigned points that has the least vertical distance. Keep in mind that by defining a vertical distance threshold, things like trees that are not part of the 3D elevation model can be eliminated.

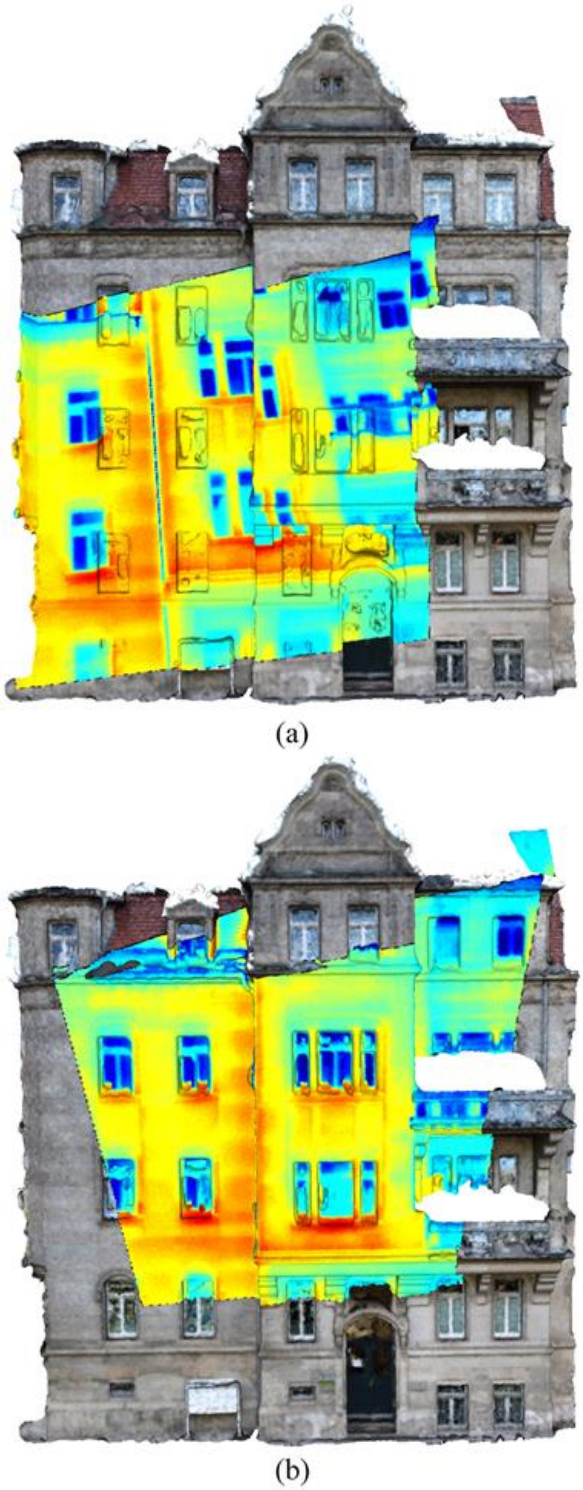

Figure 4. Texture mapping outcomes using a single sample image FGR in (a) and FGR plus image resection in (b)

Stated differently, elevation points are only incorporated into the spatial backward rendezvous process if their vertical distance is smaller than a predetermined threshold (e.g., 0.1 m), as illustrated in Figure 3. When conducting a backward intersection of the thermal image space, the initial exterior orientation parameters acquired by SfM (see Section 2.1.1 for details) are used as initial values. To enable smooth convergence of the thermal image space's backward intersection procedure, the related RGB points are transformed using the FGR coarse alignment findings. The maximum and mean reprojection errors are two examples of accuracy measures.

In this configuration, an image is deemed unsuccessful and is not used in the next texture mapping process if the average reprojection error of a thermal image surpasses 2 pixels or the maximum reprojection error exceeds 5 pixels. It is important to note that passing the maximum reprojection error is still required as an extra precaution, even though the reprojection error has been evenly distributed over all feature points following the image space rendezvous.

Figure 4 shows the texture mapping results of a single image utilizing both fine alignment (FGR with spatial segmentation, 4b) and coarse alignment (by FGR, 4a), with the latter being obviously better. Actually, depending solely on coarse alignment (FGR) results in imprecise texture mapping and inadequate baseline values. This is due to the fact that, in order for the suggested approach to converge to the global optimum, it needs a sound initial setup; otherwise, it may produce inaccurate results or local optimal solutions.

2.2 Principles of infrared thermal imaging detection

According to earlier research, the IRT method may qualitatively identify a variety of problems, including surface cracking, voids between the wall surface and the finish layer, and thermal flaws in the exterior thermal insulation layer. Nonetheless, there are still a lot of technical issues that need to be resolved before these events can be quantitatively detected and analyzed [18]. This paper employs infrared thermal imaging technology to construct an experimental platform for detection. It also establishes a three-dimensional model of infrared thermal imaging detection using ANSYS software to quantitatively investigate the impact of the external thermal insulation layer's dimensions and ambient temperature on the detection effect.

The external thermal insulation layer of the building outside can be roughly represented as an infinite single-layer flat wall because of its huge area-to-thickness ratio, and this approximation satisfies the necessary requirements [19].

$$\begin{cases} \dfrac{\partial}{\partial x}\left(\lambda \dfrac{\partial T}{\partial x}\right) = \rho c \dfrac{\partial T}{\partial t} \\ t = 0, T = T_0 \end{cases} \tag{2}$$

In what situation does $\partial \mathrm{T} / \partial x = 0$ occur when $x = d$, $\lambda \cdot \partial T / \partial x = h(T - T_e)$; λ represents the building exterior wall insulation layer's (unit $W \cdot m^{-1} \cdot {}^{\circ}C^{-1}$); T is the layer's temperature inside the building at any given point (unit °C); ρ is the layer's density (unit $\mathrm{kg} \cdot m^{-3}$); c is the layer's specific heat capacity (unit $J \cdot \mathrm{kg}^{-1} \cdot {}^{\circ}C^{-1}$); and x is the space coordinates' direction.

We may formulate the differential equation of thermal conductivity and the edge value condition as follows for the defect-free insulating layer: $\theta = T - T_a$.

$$\begin{cases} \dfrac{\partial \theta}{\partial t} = a \dfrac{\partial^2 \theta}{\partial X^2} \\ t = 0, \theta = \theta_0 = T_0 - T_{\mathrm{a}} \end{cases} \tag{3}$$

where, $a = \lambda/\rho c$ is the ambient temperature parameter in degrees Celsius, and T_a is the thermal conductivity coefficient. After replacement, $X = x/d$ is used as the coordinate variable, while $F = \theta/\theta_0$ is used as the temperature variable. The data are dimensionless.

$$\begin{cases} \dfrac{\partial F}{\partial\left(\mathrm{at}/d^2\right)} = \dfrac{\partial^2 F}{\partial X^2}, \\ t = 0, F = F_0 = 1 \end{cases} \tag{4}$$

For this simulation, the criterion Bivolt number is $B_i = hd/\lambda$. The criterion Fourier number is $F_0 = \mathrm{at}/d^2$, which is the time variable of the heat conduction process in the insulation layer after substitution. This can be stated as follows: the dimensionless coordinate variable *X*, the Bivolt number B_i, and the Fourier number F_0 function to determine the dimensionless temperature variable *F*.

$$F = g\left(F_0, B_i, X\right) \tag{5}$$

The construction surface of the insulation layer can be thought of as a defect within it, supposing that there is a finish layer on it that is minuscule in thickness. The surfaces of the building and non-building surfaces can be found by setting the surface temperatures of the insulated building surface part (T_1) and the non-building surface part (T_h) respectively.

$$T = T_1 - T_{\mathrm{h}} \tag{6}$$

Taking into account the significance of the building surface's dimensions, specifically length (*l*), width (*w*), and thickness (δ), ΔT can be represented as:

$$\Delta T = g\left(\theta_0, t, a, d, \lambda, h, l, w, \delta\right) \tag{7}$$

where, ℃ is the unit of θ_0; *s* is the unit of *t*; $m^2 \cdot s^{-1}$ is the unit of *a*; *m* is the unit of *d*; and *m* is the unit of δ.

The other physical quantities in the physical process involved in the functional connection can be stated as follows, in accordance with the fundamental idea of the magnitude analysis method (π theorem), which is to choose the four physical quantities $\Delta T, t, \lambda, d$ with the magnitude.

$$\begin{cases} \pi_1 = \dfrac{\theta_0}{\Delta T^{\alpha 1} t^{y1} \lambda^{z1} d^{w1}}, \pi_2 = \dfrac{a}{\Delta T^{\alpha 2} t^{y2} \lambda^{z2} d^{w2}} \\ \pi_3 = \dfrac{h}{\Delta T^{\alpha 3} t^{y3} \lambda^{z3} d^{w3}}, \pi_4 = \dfrac{a}{\Delta T^{a4} t^{y4} \lambda^{z4} d^{w4}} \\ \pi_5 = \dfrac{w}{\Delta T^{\alpha 5} t^{y5} \lambda^{z5} d^{w5}}, \pi_6 = \dfrac{w}{\Delta T^{a6} t^{y6} \lambda^{z6} d^{w6}} \end{cases} \tag{8}$$

Using the quantum harmony principle, each π term's exponent equals to:

$$\begin{cases} \pi_1 = \dfrac{\theta_0}{\Delta T}, \pi_2 = \dfrac{at}{d^2}, \pi_3 = \dfrac{hd}{\lambda} \\ \pi_4 = \dfrac{l}{d}, \pi_5 = \dfrac{w}{d}, \pi_6 = \dfrac{\delta}{d} \end{cases} \tag{9}$$

The resulting dimensionless equation is:

$$F\left(\frac{\theta_0}{\Delta T}, \frac{at}{d^2}, \frac{hd}{\lambda}, \frac{l}{d}, \frac{w}{d}, \frac{\delta}{d}\right) = 0 \tag{10}$$

i.e.,:

$$\Delta T = f\left(\frac{at}{d^2}, \frac{hd}{\lambda}, \frac{l}{d}, \frac{s}{d}, \frac{\delta}{d}\right) \cdot \theta_0 \tag{11}$$

where, *A* is the building surface's actual size, *C* is the surrounding air temperature, and *R* is the thermodynamic constant.

In conclusion, the size of the building surface itself and the surrounding air temperature are the primary determinants of the temperature differential between the building surface and the non-building surface area when infrared thermal imaging technology is utilized to identify the building surface of the outer insulation layer of the building wall. This provides a theoretical basis for the simulation study.

3. CONSTRUCTION AND VERIFICATION OF A FINITE ELEMENT SIMULATION MODEL

3.1 Numerical simulation of finite elements with ANSYS Fluent

Strong finite element simulation capabilities can be found in ANSYS, particularly in its subsystem. The needs of this study are satisfied by ANSYS Fluent's precise simulation of the heat transport system under natural convection and light radiation conditions meets the needs of this study. As a result, this experiment decided to create a three-dimensional model for an infrared thermal imaging assessment of the building's exterior thermal insulation layer using ANSYS Fluent.

3.2 Building exterior thermal insulation layer modeling

We selected polystyrene foam board (EPS) as our study subject because of its low thermal conductivity, superior thermal insulation performance, and affordability. EPS is a newly developed lightweight roof insulation material that is now quite popular on the market. The experiment's test samples are 50 mm thick and measure 700 mm by 650 mm in area. We simplified the irregular building surface into regular building surfaces with different dimensions to simulate the external wall insulation layer in various insulation failure situations. This is because the building surface of the insulation layer is random, and it is difficult to control the building surface dimensions (length, width, and thickness).

Numerous variables, like the refractive index of the object being tested, the surrounding temperature, the equipment's temperature range, and resolution, might impact an infrared camera's ability to detect objects. The infrared camera is very sensitive to changes in ambient temperature. The effectiveness of infrared detection will be impacted when there is a significant disparity in temperature between the equipment and the surrounding environment, or when the ambient temperature fluctuates significantly. The environmental factors are always changing throughout the actual measurement, making it challenging to record them in a timely manner. Therefore, the uncertainty of other external factors on

the experiment can be controlled to avoid the influence of the difference in the performance of the infrared camera in the experimental results by studying the trend of the influence of the main influencing factors.

The ANSYS Fluent software creates the fluid region, builds the three-dimensional heat transfer model of the building surface on the exterior insulation layer of the building exterior wall based on the actual size of the experimental material, and meshes the model as depicted in Figure 5. Next, the fluent thermal analysis is set up according to the study item and the type of the calculation problem.

Choose the natural convection technique of thermal convection: It is required to open the gravity term, specify the gravity size and direction, and assume that the gas density is incompressible because the fluid flow is driven by the density change under the gravity field. Less than 2300 is the computed Reynolds number, indicating a laminar flow state.

Establish the radiation boundary conditions by turning on the energy equation, selecting the discrete coordinate (DO) model as the thermal radiation model, and entering the radiation parameters that match the experiment's environmental parameters.

Enter the experimental material specifications. By default, the wall is adiabatic, and the boundary conditions are specified. The primary thermodynamic parameters of the polystyrene foam board are displayed in Table 1.

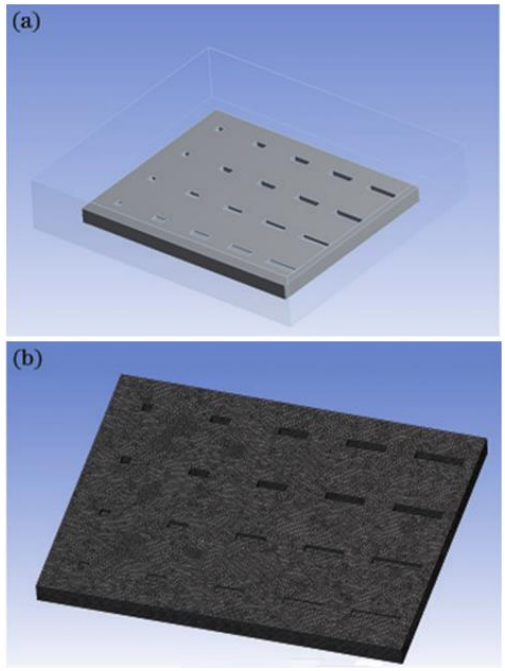

Figure 5. 3D model for polystyrene foam board IRT inspection (a) Polystyrene foam board overall schematic; (b) Model meshing

Table 1. Primary thermodynamic parameters of foam boards made of polystyrene

Length /mm	Width/mm	Thickness/mm	Specific Heat Capacity/(J·kg^{-1}·K^{-1})	Density /(kg·m^{-3})	Thermal Conductivity /(W·m^{-1}·K^{-1})	Absorption Coefficient/m^{-1}
700	650	50	1600	36	0.04	1

Launch the simulation computation to set the various operating conditions for the experiment. A short-time steady-state thermal analysis is performed first, and the iterative calculation leads to smooth temperature information as the final result. This is because the temperature field of the insulation layer is greatly affected by the time factor, and it is necessary to analyze the influence of the stable thermal load on the insulation layer insulation failure condition.

3.3 Model validation

This effort included the development of a three-dimensional heat transfer detection model to ensure the accuracy of the heat transfer model. The data from the simulation calculation was compared with field inspection data of the insulated building surface under various thickness conditions. Because of the high internal temperatures and low exterior temperatures, IRT requires a specific temperature differential between the inside and outside of the building envelope of at least 10°C in order to detect heat loss. The study was conducted at 7:00 a.m. with an outdoor temperature of 5 degrees Celsius (23 degrees Fahrenheit), which satisfies the requirement for a temperature difference. The suggested average temperature for indoor areas in Germany is 17 degrees Celsius (63 degrees Fahrenheit). The five scenarios that best capture the experimental summary of this study are "Campus 45*35meter", "Campus 45*60meter", "Campus 30*60meter", and "City 45*60meters". The camera angles on the flight pathways in (3) and (4) were examined in Experiment 2, while the architectural styles in (2) and (5) were compared in Experiment 4. "Campus 45*35meters" required more time for data collection and processing in these trials.

We chose a campus building to evaluate the usefulness of data fusion in many architectural domains. Traditional European urban construction is concentrated in urban locations, whereas modern buildings are constructed in more remote parts of the campus. Figure 6 shows the point cloud and thermal model of various building areas. Figures 6(a) and 6(b) depict the campus' RGB point cloud and thermal model, respectively. The thermal model is shown in an iron palette, with yellow representing high temperatures and purple representing low temperatures. Figures 6(c) and 6(d) illustrate the urban area's RGB point cloud and the thermal model produced from the RGB model.

3.3.1 Plateau comparison experiment

In the first experiment, we investigated various elevations between 35 and 60 meters. For these two flight heights, the Surface Averaged Vertical Distance, or SAVS, was computed and summarized. The precise findings are as follows: there are six rows for the test at 35 m altitude (rows 1, 5, 9, 13, 17, and 21) and six rows for the test at 60 m altitude (rows 2, 6, 10, 14, 18, and 22). As illustrated in Figure 6(a), these six rows correspond to six evaluations of various point cloud objects, including buildings 1, 2, 3, and 4. Table 2 provides an overview of the four structures and their surroundings, which include roads, meadows, and trees. The parameters for restricting the distance between the destination and projection points are shown in the column. Rays convey thermal imaging pixels to 3D models, where they blend into the final point

cloud models. This procedure computes the distance to the closest point in the point cloud. When the distance is beyond a certain threshold, such as 0.1, 0.2, 0.3, 0.4, or 0.5 meters, there is no connection between the projected point and any target point. The scenario in which there is no threshold is indicated by column "N". In Section 2.2, the remaining rows are set aside for other trials.

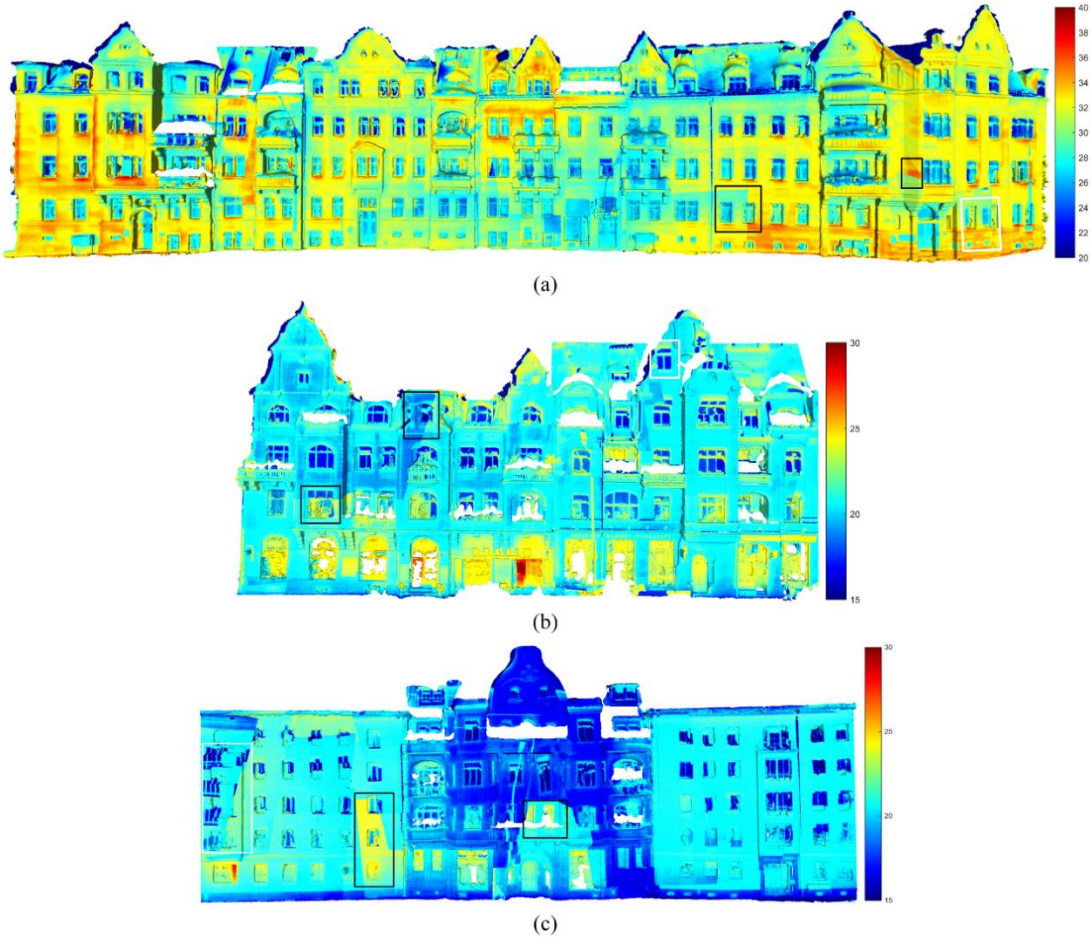

Figure 6. Campus building thermal modeling schematic

Furthermore, we provide a summary of the contact point SAVS [20] (Table 3). The data fusion techniques varied, even though the experimental setup was different. Context Capture gave the 2D coordinates of the connection points, which were immediately employed by data fusion for the connection points. However, since Context Capture does not generate issues between the 3D and 2D coordinates of the 3D point cloud model, the algorithm described in Section 2 must be utilized for the data fusion of all points. A program that overlays the data from the 2D picture onto the 3D model must be put into place.

The distribution of the other SD values is used to compute the SAV. The TL distribution with 0.01 bin sizes is displayed in Figure 7 to help visualize the distribution. The experimental "Campus45 Mesh 35m" distribution is displayed in Figure 7 (a), (b), and (c), whereas the experimental "Campus45 Mesh 60m" distribution is given in Figure 7 (d), (e), and (f). Figure 7 covers the additional tests described in Sections 2.2 and 2.3. The first column of Figure 7 depicts the distribution of points in and around all buildings, the x-axis is the probable SD value, and the y-axis is the distribution of SD values at the connection sites in prior research [21], and the SD values for all the points generated by the proposed fusion method. All data pertain to the experimental case where there is no restriction between the target and projection points, and no other thresholds such as 0.1 to 0.5 m are plotted in the data.

3.3.2 A comparison of camera angles

In experiment 2, different camera angles of 45 and 30 degrees were investigated. Table 2 presents the computed SAVS estimates from both perspectives. The 45-degree experiment contains six rows (2, 6, 10, 14, 18, and 22), while the 30-degree experiment has six columns (3, 7, 11, 15, 19, and 23). Figures 7 (d), (e), and (f) show the distribution of the Campus 45 Mesh 60 m experiment, while Figures 7 (g), (h), and (i) show the distribution of the "Campus 30 Mesh 60 m" trial.

When we initially compare Figures 7(d), (e), and (f) to Figures 7(g), (h), and (i), we can see that the 45-degree camera angle has a more dispersed distribution than the 30-degree camera angle. Furthermore, the later trial was dispersed closer to the y-axis than the former, resulting in a higher proportion of locations with lower SD values. Second, regardless of how the subpopulations and thresholds were set up, the SAVS of the first experiment was always higher than that of the second. Third, as can be seen in Figures 7(f) and 7(i), the vertical SAVS lines for each grouping in the first trial were significantly farther away from the y-axis than in the second trial. More specifically, the vertical lines in the second experiment were denser than in the first. Fourth, as the threshold was lowered in the earlier and later trials, the SAV dropped.

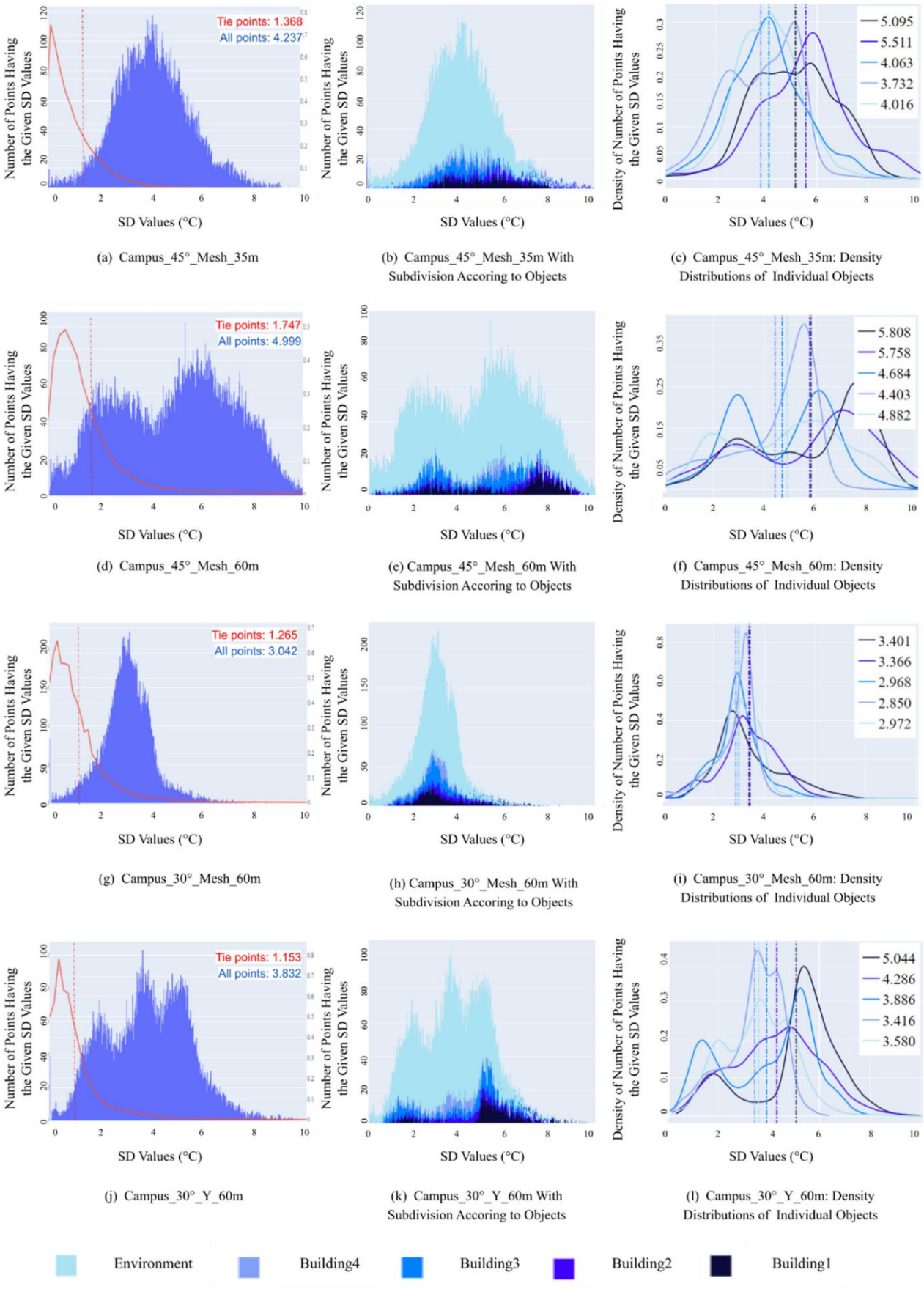

Figure 7. SD value distribution for many tests (binary size = 0.01)

3.4 Comparison of flight paths

Several flight patterns, such as a Y-shaped and cross-grid flying path, were tested in Experiment 3. Table 2 summarizes and calculates the SAV evaluations for both paths. Lines 3, 7, 11, 11, 15, 19, and 23 correspond to a cross-mesh flight, whereas lines 4, 8, 12, 16, 20, and 24 relate to a Y-shaped flight. The experimental "Campus 30° Mesh 60 m" distribution is

presented in Figures 7 (g), (h), and (i), while the experimental "Campus 30° Y 60 m" distribution is displayed in Figures 6 (j), (k), and (l).

When additional flight configurations are provided, the distribution of the grid trajectory is more concentrated than that of the Y-shaped trajectory, as demonstrated in Diagrams 7 (g), (h), and (i) against Diagrams 7 (j), (k), and (l). The second experiment's distribution was erratic. Table 2 shows that certain subgroups have two or three peaks in the distance between the target and projection points, in both experiments, the SAV is always smaller in the former. Third, the distribution in the vertical direction was more prominent in the former trial than in the later, as seen in Figures 7(i) and 7(l). Fourth, this experiment similarly showed the same phenomenon of diminishing SAVS with a decreasing threshold. Lastly, there were differences in SAVs between flight paths for contact points and all points. The SAV for grid flights (1.265) was marginally greater than the SAV for the Y path (1.53) for contact locations. Conversely, the SAV for the Y-path (3.832) was higher than the SAV for the grid-fly path (3.042) at every point.

3.5 Architectural style comparison

Tables 2 and 4 present the results of the tests conducted on campus buildings and urban buildings, and the SAVS evaluations that were computed for these two distinct building types and densities. Table 2 summarizes the experimental data for the campus region ("Campus 45 grid 60 meters"), while Table 4 summarizes the experimental data for the urban area ("City 45 grid 60 meters"). Six rows (rows 2, 6, 10, 14, 18, and 22 in Table 2) comprise the tests for the campus area, whereas six columns (columns 1, 2, 3, 4, 5, and 6 in Table 4) include the examinations for the city region. Because the university region and the city region have different architectural styles, the data fusion performance evaluation results are broken down into separate tables. Four structures in the metropolitan area were also looked into as potential targets. These six lines also correspond to six estimations for numerous point cloud groupings, including Building 1, Building 2, Building 3, Building 4, and all buildings and their environs (e.g., meadows, trees, and roads). Figures 5(c) and 5(d) show three-dimensional representations of these buildings.

Table 2. Displays the statistical information regarding the evaluation criteria applied to different tests conducted under different circumstances

	Subgroup One: Building 1							Subgroup Two: Building 2					
	Experiments	Threshold						Threshold					
		0.1	0.2	0.3	0.4	0.5	N	0.1	0.2	0.3	0.4	0.5	N
1	Campus_45° _Mesh_35m	4.955	5.007	5.062	5.075	5.095	5.096	5.308	5.388	5.449	5.499	5.508	5.510
2	Campus_45° _Mesh_60m	5.569	5.699	5.778	5.792	5.909	5.909	5.496	5.596	5.689	5.729	5.755	5.759
3	Campus_30° _Mesh_60m	3.321	3.339	3.381	3.398	3.402	3.402	3.167	3.274	3.323	3.366	3.366	3.367
4	Campus_30° _Y_60m	4.972	4.985	5.025	5.042	4.996	4.965	4.144	4.201	4.259	4.2283	4.287	4.287
	Subgroup Three: Building 3							Subgroup Four: Building 4					
	Experiments	Threshold						Threshold					
		0.1	0.2	0.3	0.4	0.5	N	0.1	0.2	0.3	0.4	0.5	N
9	Campus_45° _Mesh_35m	3.954	4.002	4.033	4.054	4.059	4.061	3.445	3.542	3.619	3.655	3.711	3.733
10	Campus_45° _Mesh_60m	4.457	4.569	4.637	4.677	4.686	4.685	4.382	4.355	4.379	4.396	4.404	4.404
11	Campus_30° _Mesh_60m	2.893	2.938	2.957	2.969	2.969	2.971	2.785	2.831	2.829	2.844	2.855	2.855
12	Campus_30° _Y_60m	3.800	3.853	3.869	3.871	3.887	3.892	3.308	3.310	3.388	3.406	3.414	3.415
	Subgroup Five: All Buildings							Subgroup Six: All Buildings with Their Surrounding Environment					
	Experiments	Threshold						Threshold					
		0.1	0.2	0.3	0.4	0.5	N	0.1	0.2	0.3	0.4	0.5	N
17	Campus_45° _Mesh_35m	4.505	4.557	4.612	4.639	4.655	4.658	4.063	4.144	4.179	4.224	4.236	4.899
18	Campus_45° _Mesh_60m	5.044	5.147	5.211	5.247	5.257	5.257	4.806	4.898	4.961	4.995	4.998	4.998
19	Campus_45° _Mesh_60m	3.058	3.118	3.151	3.162	3.166	3.166	2.944	2.955	3.022	3.040	3.039	3.039
20	Campus_30° _Y_60m	4.161	4.203	4.233	4.255	4.259	5.259	3.739	3.797	3.815	3.829	3.833	3.833

Table 3. Collar point SAV statistics for several trials carried out in various environments

Experiment	Campus_45°_Mesh_35m	Campus_45°_Mesh_60m	Campus_30°_Mesh_60m	Campus_30°_Y_60m	City_45°_Mesh_60m
SAV	1.371	1.745	1.366	1.149	1.192

Table 4. Statistical parameters of assessment standards for various tests carried out in various environments

	SAV						
	Threshold Grouping	0.1	0.2	0.3	0.4	0.5	N
1	Building 1	2.879	3.959	4.007	4.052	4.039	4.039
2	Building 2	3.372	3.427	3.473	3.501	3.506	3.506
3	Building 3	3.822	3.882	3.935	3.959	3.955	3.955
4	Building 4	3.409	3.681	3.489	3.506	3.503	3.503
5	All buildings	3.607	3.449	3.721	3.739	3.731	3.734
6	All buildings and their surroundings	3.618	3.397	3.734	3.759	3.757	3.756

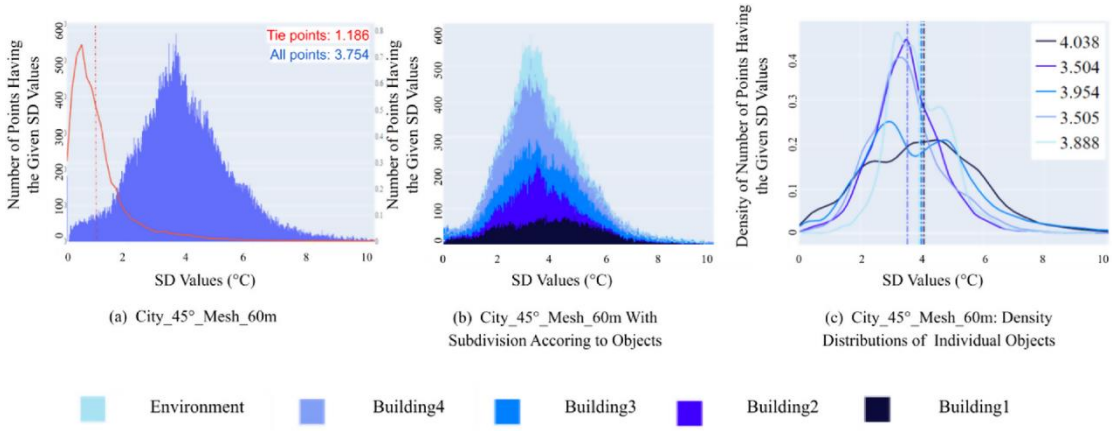

Figure 8. SD value distribution for various experiments

Figure 7 presents the findings of the experiment "City_45 grid 60m," which is contrasted with the experiment "Campus 45 grid 60m" in Figure 7 to visualize the distribution characteristics. Figure 8 (a), (b), and (c) depict scenarios without a distance standard between the target point and the projection point, which correspond to Figures 7 (d), (e), and (f). However, the case with a distance threshold of 0.1-0.5 m is not shown. Figure 7 compares the outcomes of the experiments "Campus 45 grid 60 m" with "City 45 grid 60 m."

We only looked into the overall effectiveness of the data fusion methods for the campus and urban region because Building 1 on the campus and Building 1 in the urban area have completely distinct architectural styles and volumes that make them impossible to compare directly. It can be observed that the distribution of the campus experiment is more diffused than that of the city-region experiment with the other flight configurations fixed by comparing. In the campus experiments, the vertical lines that represented the SAV of the various subgroups were similarly more spread and located farther away from the Y-axis (Figures 7(f) and 8(c)). Furthermore, as the thresholds were lowered, the SAV values for the urban area experiments also declined.

4. CONCLUSION

This study examined the properties of heat transmission on building surfaces and the exterior building insulation using IRT in conjunction with finite element numerical modeling (ANSYS Fluent). Understanding how building surfaces affect heat transfer performance is made easier with the help of ANSYS Fluent software, which accurately simulates complicated heat transfer systems. The variations in settings and architectural types could be the cause of this. As the distance threshold was lowered, the SAV values declined as well, although the decrease in the campus area was less pronounced, suggesting a more stable detection.

In order to support a greater variety of building types and intricate climatic circumstances, the application of IRT can be further enhanced in the future to increase the model's accuracy and computing efficiency. To enhance the use of IRT in the detection of building surfaces on building facades, it is also possible to investigate the impact of additional influencing elements, such as variations in ambient temperature and measurement accuracy, on the detection findings.

ACKNOWLEDGEMENTS

This paper was supported by the Natural Science Foundation of Inner Mongolia Autonomous Region (Grant No.: 2021MS05008) and the Basic Scientific Research Business Expense Project of Colleges and Universities Directly under Inner Mongolia Autonomous Region (Grant No.: JY20220216).

REFERENCES

[1] Keo, S.A., Szymanik, B., Le Roy, C., Brachelet, F., Defer, D. (2023). Defect detection in CFRP concrete reinforcement using the microwave infrared thermography (MIRT) method—A Numerical Modeling and Experimental Approach. Applied Sciences, 13(14): 8393. https://doi.org/10.3390/app13148393

[2] Lin, Z., Wang, Z., Zhu, Y., Li, Z., Qin, H. (2024). Text sentiment detection and classification based on integrated learning algorithm. Applied Science and Engineering Journal for Advanced Research, 3(3): 27-33. https://doi.org/10.5281/zenodo.11516191

[3] Kim, H., Lamichhane, N., Kim, C., Shrestha, R. (2023). Innovations in building diagnostics and condition monitoring: A comprehensive review of infrared thermography applications. Buildings, 13(11): 2829.

https://doi.org/10.3390/buildings13112829
[4] Afzal, M.K., Zikria, Y.B., Mumtaz, S., Rayes, A., Al-Dulaimi, A., Guizani, M. (2018). Unlocking 5G spectrum potential for intelligent IoT: Opportunities, challenges, and solutions. IEEE Communications Magazine, 56(10): 92-93. https://doi.org/10.1109/MCOM.2018.8493125
[5] Zhang, C., Zou, Y., Dimyadi, J., Chang, R. (2023). Thermal-textured BIM generation for building energy audit with UAV image fusion and histogram-based enhancement. Energy and Buildings, 301: 113710. https://doi.org/10.1016/j.enbuild.2023.113710
[6] Guo, Z., Yu, K., Kumar, N., Wei, W., Mumtaz, S., Guizani, M. (2022). Deep-distributed-learning-based POI recommendation under mobile-edge networks. IEEE Internet of Things Journal, 10(1): 303-317. https://doi.org/10.1109/JIOT.2022.3202628
[7] Motayyeb, S., Samadzedegan, F., Javan, F.D., Hosseinpour, H. (2023). Fusion of UAV-based infrared and visible images for thermal leakage map generation of building facades. Heliyon, 9(3): e14551. https://doi.org/10.1016/j.heliyon.2023.e14551
[8] Liao, H., Zhou, Z., Liu, N., Zhang, Y., Xu, G., Wang, Z., Mumtaz, S. (2022). Cloud-edge-device collaborative reliable and communication-efficient digital twin for low-carbon electrical equipment management. IEEE Transactions on Industrial Informatics, 19(2): 1715-1724. https://doi.org/10.1109/TII.2022.3194840
[9] Einizinab, S., Khoshelham, K., Winter, S., Christopher, P., Fang, Y., Windholz, E., Hu, S. (2023). Enabling technologies for remote and virtual inspection of building work. Automation in Construction, 156: 105096. https://doi.org/10.1016/j.autcon.2023.105096
[10] Pan, J., Ye, N., Yu, H., Hong, T., Al-Rubaye, S., Mumtaz, S., Chih-Lin, I. (2022). AI-driven blind signature classification for IoT connectivity: A deep learning approach. IEEE Transactions on Wireless Communications, 21(8): 6033-6047. https://doi.org/10.1109/TWC.2022.3145399
[11] Afzal, M.K., Zikria, Y.B., Mumtaz, S., Rayes, A., Al-Dulaimi, A., Guizani, M. (2018). Unlocking 5G spectrum potential for intelligent IoT: Opportunities, challenges, and solutions. IEEE Communications Magazine, 56(10): 92-93. https://doi.org/10.1109/MCOM.2018.8493125
[12] Zhang, C., Wang, F., Zou, Y., Dimyadi, J., Guo, B.H., Hou, L. (2023). Automated UAV image-to-BIM registration for building façade inspection using improved generalised Hough transform. Automation in Construction, 153: 104957. https://doi.org/10.1016/j.autcon.2023.104957
[13] Guo, Z., Yu, K., Kumar, N., Wei, W., Mumtaz, S., Guizani, M. (2022). Deep-distributed-learning-based POI recommendation under mobile-edge networks. IEEE Internet of Things Journal, 10(1): 303-317. https://doi.org 10.1109/JIOT.2022.3202628
[14] Tan, Y., Yi, W., Chen, P., Zou, Y. (2024). An adaptive crack inspection method for building surface based on BIM, UAV and edge computing. Automation in Construction, 157: 105161. https://doi.org/10.1016/j.autcon.2023.105161
[15] Radwan, A., Huq, K.M.S., Mumtaz, S., Tsang, K.F., Rodriguez, J. (2016). Low-cost on-demand C-RAN based mobile small-cells. IEEE Access, 4: 2331-2339. https://doi.org/10.1109/ACCESS.2016.2563518
[16] Wu, J., Shi, Y., Wang, H., Wen, Y., Du, Y. (2023). Surface defect detection of Nanjing city wall based on UAV oblique photogrammetry and TLS. Remote Sensing, 15(8): 2089. https://doi.org/10.3390/rs15082089
[17] Bustos, N., Mashhadi, M., Lai-Yuen, S.K., Sarkar, S., Das, T.K. (2023). A systematic literature review on object detection using near infrared and thermal images. Neurocomputing, 560: 126804. https://doi.org/10.1016/j.neucom.2023.126804
[18] Mayer, Z., Epperlein, A., Vollmer, E., Volk, R., Schultmann, F. (2023). Investigating the quality of UAV-based images for the thermographic analysis of buildings. Remote Sensing, 15(2): 301. https://doi.org/10.3390/rs15020301
[19] Yang, X., Guo, R., Li, H. (2023). Comparison of multimodal RGB-thermal fusion techniques for exterior wall multi-defect detection. Journal of Infrastructure Intelligence and Resilience, 2(2): 100029. https://doi.org/10.1016/j.iintel.2023.100029
[20] ElSheikh, A., Abu-Nabah, B.A., Hamdan, M.O., Tian, G.Y. (2023). Infrared camera geometric calibration: A review and a precise thermal radiation checkerboard target. Sensors, 23(7): 3479. https://doi.org/10.3390/s23073479
[21] Shao, Z., Deng, R., Zhang, G., Li, Y., Tang, X., Zhang, W. (2023). 3D thermal mapping of smoldering coal gangue pile fires using airborne thermal infrared data. Case Studies in Thermal Engineering, 48: 103146. https://doi.org/10.1016/j.csite.2023.103146